MOX–Report No. 44/2014

Active contraction of the cardiac ventricle and distortion of the microstructural architecture

PEZZUTO, S.; AMBROSI,D.

Active contraction of the cardiac ventricle and distortion of the microstructural architecture

S. Pezzuto[1] and D. Ambrosi[2*]

[1]*Simula Research Laboratory, 1325 Lysaker, Norway*
[2]*MOX–Politecnico di Milano, piazza Leonardo da Vinci 32, 20133 Milano, Italy*

SUMMARY

The shortening of the myocardial fibers is the microstructural engine that produces the contraction of the cardiac muscle. The complex interplay between fibers shortening and elastic macroscopic strain is functional to the ejection of blood into the pulmonary and arterial networks. Here we address the contraction of the left ventricle in a finite elasticity framework, adopting the "prolate ellipsoid" geometry and the invariants–based strain energy proposed by Holzapfel and Ogden, where the mechanical role of fibers and sheets is accounted for. We show that a microstructurally motivated mathematical model of active strain type reproduces the main indicators of normal cardiac function along the whole PV-loop without introduction of any further *ad hoc* law. The bare–bones mathematical model depends on one measurable parameter only, i.e. the shortening ratio of the sarcomere units, which we assume to be nearly independent on the prestretch. Strict enforcement of incompressibility and novel treatment of boundary conditions are shown to be crucial to simulate the correct muscle torsion. Copyright © 0000 John Wiley & Sons, Ltd.

Received . . .

INTRODUCTION

From a structural point of view, the myocardium can be classified as a hyperelastic orthotropic material, characterized by two mutually orthogonal directions of mechanical relevance: the fibers and the sheets [1, 2]. In this work we focus on the left ventricle, the cardiac chamber that produces the largest work. In systole the fibers contract, actively producing a strain of the cardiac wall that shrinks the inner volume and, at the aortic valve opening, the blood is ejected. In the filling phase of the cardiac cycle, the elastic strain in the cardiac wall is released, thus favoring the inflow of blood that eventually deforms the chamber passively under the action of the venous pressure difference.

In the present paper we focus on the (active) structural mechanics of the cardiac muscle. Among the many material models available in the literature [3, 4, 5], the hyperelastic strain energy proposed by Holzapfel and Ogden [6] to describe the mechanics of the passive myocardium is gaining an increasing interest. Its simple invariant–based formulation, the small set of material parameters invoked and its suitable mathematical properties make it particularly attractive for numerical simulations. Even more important, the material parameters of the model can, in principle, be determined on the basis of standard biaxial and shear stress–strain tests [7, 8] without an *ad hoc* fitting in the specific application. Recent papers have already addressed the use of this model to real geometry simulations [9, 10, 8, 11, 12, 13, 14, 15], while a detailed discussion about the numerical implementation and the performance of the model in test cases has been discussed elsewhere [16].

In this work we study the performance of the Holzapfel–Ogden strain energy along the whole PV-loop for physiological values of pressure. In our bare–bones approach, we dictate a constant

---

*Correspondence to: Simula Research Laboratory, 1325 Lysaker, Norway. E-mail: simonep@simula.no

shortening of the microstructure in the macroscopic model, independent of the strain, and we compute the strain and stress in myocardium. The numerical model, that has been tested versus elementary geometries in a past work [16], is here applied to the simulation of the full PV–loop in a prolate ellipsoid, using a tetrahedral unstructured mesh. We adopt novel, very weak, boundary conditions that enforce null average displacement and null average rotation only. In the same vein, the constant-volume constraint that applies in the filled chamber during the isochoric contraction and relaxation is enforced at a variational level with a Lagrange multiplier that turns out to be the produced blood pressure.

The performance of the method is discussed in terms of its numerical stability and versus its ability to reproduce in a correct physiological range a number of indicators of normal cardiac functionality: passive filling volume, thickening of the wall, elongation and shortening along the main axis, muscle torsion, stroke volume and strain measures. Intriguingly, the nonlinearity of the material properties is sufficient by itself to reproduce the expected growth of the produced force versus the prestretch.

1. BACKGROUND AND NOTATION

Given a continuum body $\mathfrak{B}$, we consider a reference configuration χ_0, and a generally unknown actual configuration χ as functions from $\mathfrak{B}$ to $\mathbb{R}^3$. The reference and actual placements of the body in $\mathbb{R}^3$ are $\Omega_0 := \chi_0(\mathfrak{B})$ and $\Omega := \chi(\mathfrak{B})$, respectively; given $\mathfrak{p} \in \mathfrak{B}$, $\mathbf{X} = \chi_0(\mathfrak{p}) \in \Omega_0$, and $\mathbf{x} = \chi(\mathfrak{p}) \in \Omega$, so that a deformation is the map:

$$\boldsymbol{\varphi} = \chi \circ \chi_0^{-1}, \qquad \boldsymbol{\varphi} \colon \Omega_0 \ni \mathbf{X} \mapsto \mathbf{x} = \chi\big(\chi_0^{-1}(\mathbf{X})\big) \in \Omega.$$

We assume $\boldsymbol{\varphi}$ to be a diffeomorphism from Ω_0 to Ω, whose derivative is the tensor gradient of deformation:

$$\mathsf{F}(\mathbf{X}) := \frac{\partial \boldsymbol{\varphi}}{\partial \mathbf{X}}, \qquad [\mathsf{F}_{ij}] = \frac{\partial \varphi_i}{\partial X_j}, \qquad i, j \in \{1, 2, 3\}.$$

Denoting by $\mathrm{Lin}^+(\mathbb{R}^3)$ the vector space of all linear transformations from $\mathbb{R}^3$ to $\mathbb{R}^3$ with strictly positive determinant, we define the set of admissible configuration as follows:

$$\mathscr{C} = \Big\{ \boldsymbol{\varphi} \colon \Omega_0 \to \Omega \text{ such that } J := \det(\mathsf{F}) > 0 \text{ and } \boldsymbol{\varphi}|_{\partial_{\mathrm{D}} \Omega_0} = \mathbf{g} \Big\}, \tag{1}$$

where $\mathbf{g}$ is a given displacement. In what follows we further assume that $\partial_{\mathrm{D}} \Omega_0$ and $\partial_{\mathrm{N}} \Omega_0$ are open subsets (with respect to induced the topology) of the boundary on which essential and natural boundary conditions apply, respectively.

As usual, we define the right and left Cauchy–Green and Green strain tensors as follows:

$$\mathsf{C} := \mathsf{F}^{\mathsf{T}} \mathsf{F}, \qquad \mathsf{B} := \mathsf{F} \mathsf{F}^{\mathsf{T}}, \qquad \text{and} \qquad \mathsf{E} := \frac{1}{2} (\mathsf{C} - \mathsf{I}),$$

respectively.

The stress state of the body is described, on the actual configuration, by the Cauchy stress tensor T; thanks to the Piola transformation, we can also write the first and second Piola–Kirchhoff tensors:

$$\mathsf{P} := J \mathsf{T} \mathsf{F}^{-\mathsf{T}}, \qquad \mathsf{S} := \mathsf{F}^{-1} \mathsf{P} = J \mathsf{F}^{-1} \mathsf{T} \mathsf{F}^{-\mathsf{T}}. \tag{2}$$

The constitutive relation between the stress T and F is prescribed within the hyperelasticity framework; it exists a function $\mathcal{W} \colon \Omega_0 \times \mathrm{Lin}^+ \to \mathbb{R}$, called strain–energy density function, such that, for every admissible F, the following relationship holds:

$$\frac{\partial \mathcal{W}}{\partial \mathsf{F}} : \dot{\mathsf{F}} = \mathsf{P} : \dot{\mathsf{F}}, \qquad \text{or, equivalently} \qquad 2 \frac{\partial \widehat{\mathcal{W}}}{\partial \mathsf{C}} : \dot{\mathsf{C}} = \mathsf{S} : \dot{\mathsf{C}}, \tag{3}$$

where $\widehat{\mathcal{W}}(\mathbf{X}, \mathsf{C}) = \widehat{\mathcal{W}}(\mathbf{X}, \mathsf{F}^\mathsf{T}\mathsf{F}) = \mathcal{W}(\mathbf{X}, \mathsf{F})$. As usual, $\mathcal{W}$ must be objective, which implies that:

$$\mathcal{W}(\mathbf{X}, \mathsf{F}) = \mathcal{W}(\mathbf{X}, \mathsf{QF}), \qquad \text{for all } \mathsf{Q} \in \mathrm{Rot},$$

where $\mathrm{Rot} = \{\mathsf{Q} \in \mathrm{Lin}\colon \mathsf{QQ}^\mathsf{T} = \mathsf{I}\}$. In this respect, we directly use $\widehat{\mathcal{W}}$ in order to automatically satisfy the objectivity.

In the hyperelasticity framework, the elastic equilibrium can be characterized as a minimization problem:

$$\min_{\boldsymbol{\varphi} \in V} \int_{\Omega_0} \widehat{\mathcal{W}}(\mathbf{X}, \mathsf{C}) \, \mathrm{d}V \tag{4}$$

where suitable boundary conditions and possible constraints are to be enforced. We need some extra restriction on the deformations and the functional itself, in order to establish that at least a minimum exists. A typical choice of the function space is $V := \mathscr{C} \cap \mathrm{W}^{1,s}(\Omega_0; \mathbb{R}^3)$, $s > \frac{3}{2}$, and the polyconvexity of the strain–energy density function is usually the characterization required for the well–posedness of the minimization problem [17, 18].

A material is incompressible when $J := \det \mathsf{F} = 1$. The explicit form of the Cauchy stress is obtained from (2) and (3), after properly restricting the set of admissible $\dot{\mathsf{C}}$:

$$\mathsf{T} = J^{-1}\mathsf{F}\left(2\frac{\partial\widehat{\mathcal{W}}}{\partial\mathsf{C}} - pJ\mathsf{C}^{-1}\right)\mathsf{F}^\mathsf{T} = 2J^{-1}\mathsf{F}\frac{\partial\widehat{\mathcal{W}}}{\partial\mathsf{C}}\mathsf{F}^\mathsf{T} - p\mathsf{I}, \tag{5}$$

where $p \in Q = \mathrm{L}^2(\Omega_0)$ is an unknown scalar field [19]. In this case, the minimization problem (4) can be recast to a saddle–point problem:

$$\min_{\boldsymbol{\varphi} \in V} \max_{p \in Q} \int_{\Omega_0} \left\{\widehat{\mathcal{W}}(\mathbf{X}, \mathsf{C}) - p(J-1)\right\} \mathrm{d}V. \tag{6}$$

2. PASSIVE MECHANICS

Given a hyperelastic material with strain–energy function $\widehat{\mathcal{W}}(\mathbf{X}, \mathsf{C})$, we suppose that, for a fixed point $\mathbf{X} \in \Omega_0$, the following local invariance property is verified:

$$\widehat{\mathcal{W}}(\mathsf{C}) = \widehat{\mathcal{W}}(\mathsf{QCQ}^\mathsf{T}), \qquad \text{for every } \mathsf{Q} \in \mathscr{G} \subseteq \mathrm{Rot}.$$

The relation means that the strain–energy is the same if we change the reference configuration through the rotation Q, for any given deformation C (and so is the elastic response of the considered material). It is possible to show that $\mathscr{G}$ is a subgroup of Rot, with respect to the usual composition law [20]. In other words, $\widehat{\mathcal{W}}$ is invariant under the action of the material symmetry group $\mathscr{G}$. The characterization of $\mathscr{G}$ defines the possible anisotropic properties of the material: if $\mathscr{G} \equiv \mathrm{Rot}$, the material is *isotropic*, while if $\mathscr{G}$ is a proper subgroup of Rot, the material is *anisotropic*.

Given an orthonormal ternary $\{\mathbf{f}_\circ, \mathbf{s}_\circ, \mathbf{n}_\circ\}$, in the reference configuration, for an *orthotropic* material the strain–energy is invariant with respect to rotations around any versor of the triplet. This defines [21]:

$$\mathscr{G}_{\mathrm{orth}} = \left\{\mathsf{Q} \in \mathrm{Rot}\colon \mathsf{Q}(\mathbf{m} \otimes \mathbf{m})\mathsf{Q}^\mathsf{T} = \mathbf{m} \otimes \mathbf{m}, \text{ for } \mathbf{m} \in \{\mathbf{f}_\circ, \mathbf{s}_\circ, \mathbf{n}_\circ\}\right\}.$$

In our specific case, $\mathbf{f}_\circ$ represents the local muscle fiber direction, while $\mathbf{s}_\circ$ lies in the sheet surface and is orthogonal to $\mathbf{f}_\circ$. By definition $\mathbf{n}_\circ = \mathbf{f}_\circ \wedge \mathbf{s}_\circ$ is normal of the local sheet.

The strain energy proposed in [6] is based on the following reduced set of invariants:

$$\Upsilon_{\mathsf{HO}} = \left\{\mathcal{I}_1, \mathcal{I}_{4,\mathbf{f}_\circ}, \mathcal{I}_{4,\mathbf{s}_\circ}, \mathcal{I}_{8,\mathbf{f}_\circ\mathbf{s}_\circ}\right\}, \tag{7}$$

where:

$$\mathcal{I}_1(\mathsf{C}) = \mathrm{tr}\,\mathsf{C}, \qquad \mathcal{I}_{4,\mathbf{a}}(\mathsf{C}) = \mathbf{a} \cdot \mathsf{C}\mathbf{a}, \qquad \mathcal{I}_{8,\mathbf{a}\mathbf{b}}(\mathsf{C}) = \mathbf{a} \cdot \mathsf{C}\mathbf{b}.$$

The material is assumed to be incompressible, thus the dependence on $\operatorname{tr} C^3$, which is related to $\det C$ and the other invariants through the Cayley–Hamilton theorem, is neglected. Moreover, the dependency on the quadratic terms is (partially) fulfilled by $\mathcal{I}_{8,\mathbf{f}_\circ\mathbf{s}_\circ}$, since a relationship can be established between them [22].

From a kinematic viewpoint, all the invariants have a clear interpretation: for instance, $\mathcal{I}_{4,\mathbf{a}}$ is the square of the local stretch along the direction $\mathbf{a}$, while $\mathcal{I}_{8,\mathbf{ab}}$ is related to the angle spanned by the vectors $F\mathbf{a}$ and $F\mathbf{b}$, in the actual configuration, supposing that $\mathbf{a}$ and $\mathbf{b}$ are orthogonal.

A further hypothesis is the additive splitting of the strain–energy, thus separating the contributions of each specific deformation measure to the total energy:

$$
\begin{aligned}
\widehat{\mathcal{W}}(C) &= \widetilde{\mathcal{W}}(\mathcal{I}_1, \mathcal{I}_{4,\mathbf{f}_\circ}, \mathcal{I}_{4,\mathbf{s}_\circ}, \mathcal{I}_{8\mathbf{f}_\circ\mathbf{s}_\circ}) \\
&= \widetilde{\mathcal{W}}_1(\mathcal{I}_1) + \widetilde{\mathcal{W}}_{4,\mathbf{f}_\circ}(\mathcal{I}_{4,\mathbf{f}_\circ}) + \widetilde{\mathcal{W}}_{4,\mathbf{s}_\circ}(\mathcal{I}_{4,\mathbf{s}_\circ}) + \widetilde{\mathcal{W}}_{8,\mathbf{f}_\circ\mathbf{s}_\circ}(\mathcal{I}_{8,\mathbf{f}_\circ\mathbf{s}_\circ}).
\end{aligned}
\tag{8}
$$

Besides the mathematical reasons behind this simplification, there is also an experimental argument: it is easier to identify the corresponding material parameters from experiments.

The specific form of each term is of exponential type:

$$
\widetilde{\mathcal{W}}_1(\mathcal{I}_1) = \frac{a}{2b}\left[e^{b(\mathcal{I}_1-3)}-1\right], \qquad\qquad \widetilde{\mathcal{W}}_{4,\mathbf{f}_\circ}(\mathcal{I}_{4,\mathbf{f}_\circ}) = \frac{a_\mathsf{f}}{2b_\mathsf{f}}\left[e^{b_\mathsf{f}((\mathcal{I}_{4,\mathbf{f}_\circ}-1)_+)^2}-1\right],
$$

$$
\widetilde{\mathcal{W}}_{4,\mathbf{s}_\circ}(\mathcal{I}_{4,\mathbf{s}_\circ}) = \frac{a_\mathsf{s}}{2b_\mathsf{s}}\left[e^{b_\mathsf{s}((\mathcal{I}_{4,\mathbf{s}_\circ}-1)_+)^2}-1\right], \qquad \widetilde{\mathcal{W}}_{8,\mathbf{f}_\circ\mathbf{s}_\circ}(\mathcal{I}_{8,\mathbf{f}_\circ\mathbf{s}_\circ}) = \frac{a_\mathsf{fs}}{2b_\mathsf{fs}}\left[e^{b_\mathsf{fs}\mathcal{I}_{8,\mathbf{f}_\circ\mathbf{s}_\circ}^2}-1\right],
$$

where $(\cdot)_+$ denotes the positive part of the argument.

Thanks to (5) we can compute the explicit form of the Cauchy stress tensor T

$$
\begin{aligned}
T =\ & ae^{b(\mathcal{I}_1-3)}B - p\mathsf{I} \\
& + 2\,a_\mathsf{f}(\mathcal{I}_{4,\mathbf{f}_\circ}-1)_+ e^{b_\mathsf{f}((\mathcal{I}_{4,\mathbf{f}_\circ}-1)_+)^2}\,\mathbf{f}\otimes\mathbf{f} + 2\,a_\mathsf{s}(\mathcal{I}_{4,\mathbf{s}_\circ}-1)_+ e^{b_\mathsf{s}((\mathcal{I}_{4,\mathbf{s}_\circ}-1)_+)^2}\,\mathbf{s}\otimes\mathbf{s} \\
& + a_\mathsf{fs}\mathcal{I}_{8,\mathbf{f}_\circ\mathbf{s}_\circ}e^{b_\mathsf{fs}\mathcal{I}_{8,\mathbf{f}_\circ\mathbf{s}_\circ}^2}\,(\mathbf{f}\otimes\mathbf{s}+\mathbf{s}\otimes\mathbf{f}),
\end{aligned}
\tag{9}
$$

where $\mathbf{f} = F\mathbf{f}_\circ$ and $\mathbf{s} = F\mathbf{s}_\circ$. It can be observed that the assumptions made on the symmetry of the material, and in particular on its microstructure, reflect in the tensorial form of the Cauchy stress tensor: the isotropic contribution accounts for the extracellular matrix, while the anisotropic terms play a role along the fibers and the sheets, or when the deformation changes the angle between the two.

Following [6], the strain energy (2) is consistent with standard inequalities required from considerations of convexity, strong ellipticity and material stability. However, it is worth mentioning that the anisotropic terms associated to $\mathcal{I}_{4,\mathbf{f}_\circ}$ and $\mathcal{I}_{4,\mathbf{s}_\circ}$ needs to be turned off under compression, i.e. when $\mathcal{I}_{4,\mathbf{f}_\circ} < 1$ and $\mathcal{I}_{4,\mathbf{s}_\circ} < 1$, respectively, in agreement with the heuristic idea that physically a fiber is not able to bear load in compressive regime.

3. ACTIVE CONTRACTION

The myocardium is mainly composed by cardiac myocytes, arranged along fibers and sheets, plus a smaller component of collagen and elastin. The passive properties of the material are well reproduced by a strain energy of structural type, like the one introduced in the section above, where the material parameters can be identified on the basis of standard experiments: apply a load, measure the strain and fit the data. However living matter owns the special ability to produce motions even tough there are no external forces that act: in particular the cardiac fibers shorten to eject the blood.

This peculiar property of living matter can be studied with quite a detail at a cell level. A stress–strain relation can be measured when a myocyte is stretched over its resting length and no electric stimulus is applied: this is the passive force. Conversely, during an isometric test an electrically stimulated cardiomyocyte kept at fixed length produces a tension that can be associated to an active

force that cooperates (with a non-trivial feedback) with the passive one. In a real tissue the two contributions concur, together with the other components of the cardiac wall (collagen, elastin), to produce the macroscopic active behavior.

We account for the activation of the cardiac muscle as a change in the reference (relaxed) configuration of the body or, in other words, a control in strain of the microstructure. We carry out a multiplicative decomposition of the deformation gradient tensor into an elastic deformation F_e times an active distortion F_a [23]:

$$\mathsf{F} = \mathsf{F}_e\mathsf{F}_a,$$

where the factor F_a has to be constitutively prescribed.
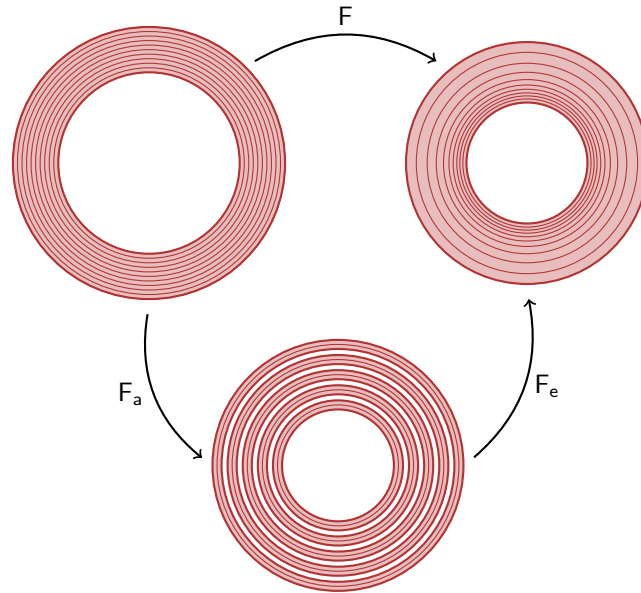
Figure 1. Pictorial view of the active strain approach: the active distortion of the fibers F_a does not preserve the integrity of the material and incompatibility is recovered by the elastic (energy storing) term F_e.

The idea, sketched in Figure 1 is the following: an inelastic dynamics, dictated by biochemical and biophysical processes, locally changes the length and the shape of the fibers, i.e. the microstructure; then, an elastic deformation F_e accommodates the material in order to preserve the compatibility of the deformation F. The physiological basis of the approach resides in the contractile units of the myocytes: the sarcomeres shorten because of the sliding filaments of the actin–myosin molecular motor, and this shortening is encoded by F_a, hence the fictitious intermediate placement determined by F_a is the new reference configuration for the elastic deformation.

The strain–energy density is a function of F_e only, the active deformation F_a being a fully dissipative process; the saddle–point problem (6) rewrites as follows:

$$\min_{\boldsymbol{\varphi}\in V} \max_{p\in Q} \int_{\Omega_0} \left\{ \widehat{\mathcal{W}}(\mathsf{F}_a^{-\mathsf{T}}\mathsf{C}\mathsf{F}_a^{-1}) - p\,(JJ_a^{-1} - 1) \right\} J_a\,\mathrm{d}V, \tag{10}$$

where $J_a = \det\mathsf{F}_a$. If the saddle point exists, the first variation of the functional in (10) must be null for every admissible variation $(\boldsymbol{\eta}, q) \in \mathcal{T}_{\boldsymbol{\varphi}}V \times Q$:

$$\int_{\Omega_0} \left[2J_a\mathsf{F}_a^{-1}\frac{\partial\widehat{\mathcal{W}}(\mathsf{C}_e)}{\partial\mathsf{C}_e}\mathsf{F}_a^{-\mathsf{T}} - p\,J\mathsf{C}^{-1} \right] : \mathrm{sym}(\mathsf{F}^\mathsf{T}\,\mathrm{GRAD}\,\boldsymbol{\eta})\,\mathrm{d}V - \int_{\Omega_0} q\,(J - J_a)\,\mathrm{d}V = 0.$$

The 2$^{\text{st}}$ Piola–Kirchhoff and the Cauchy stress tensors are, respectively:

$$\mathsf{S} = 2J_a\mathsf{F}_a^{-1}\frac{\partial\widehat{\mathcal{W}}(\mathsf{C}_e)}{\partial\mathsf{C}_e}\mathsf{F}_a^{-\mathsf{T}} - p\,J\mathsf{C}^{-1}, \qquad \mathsf{T} = \mathsf{F}_e\frac{\partial\mathcal{W}(\mathsf{F}_e)}{\partial\mathsf{F}_e}\mathsf{F}_e^\mathsf{T} - J_a^{-1}p\,\mathsf{I}.$$

If no activation is triggered, then $\mathsf{F_a} = \mathsf{I}$ and $\mathsf{F_e} = \mathsf{F}$, and the purely passive behavior of the material is recovered. If the strain energy satisfies the conditions illustrated in Section 2 then the Piola stress tensor is strongly elliptic, thus ensuring local existence and uniqueness of the solution.

The tensorial form of the active Cauchy stress is dictated by $\mathsf{F_a}$ through the strain–energy form as well. A transversely isotropic and isochoric choice might be

$$\mathsf{F_a} = (1 - \gamma)\mathbf{f_\circ} \otimes \mathbf{f_\circ} + \frac{1}{\sqrt{1 - \gamma}}\Big(\mathsf{I} - \mathbf{f_\circ} \otimes \mathbf{f_\circ}\Big). \tag{11}$$

as supported by the physiological observation that during a contraction myocytes do not change their volume significantly [24]. The explicit form of the invariants of $\mathsf{C_e}$ with the respect to the invariants of C easily follows from (11):

$$\mathcal{I}_1^{\mathrm{e}} = (1 - \gamma)\mathcal{I}_1 + \frac{1 - (1 - \gamma)^3}{(1 - \gamma)^2}\mathcal{I}_{4,\mathbf{f_\circ}}, \qquad \mathcal{I}_{4,\mathbf{f_\circ}}^{\mathrm{e}} = \frac{1}{(1 - \gamma)^2}\mathcal{I}_{4,\mathbf{f_\circ}},$$

$$\mathcal{I}_{4,\mathbf{s_\circ}}^{\mathrm{e}} = (1 - \gamma)\mathcal{I}_{4,\mathbf{s_\circ}}, \qquad \mathcal{I}_{8,\mathbf{f_\circ}\mathbf{s_\circ}}^{\mathrm{e}} = \frac{1}{\sqrt{1 - \gamma}}\mathcal{I}_{8,\mathbf{f_\circ}\mathbf{s_\circ}}.$$

The coefficient γ here does not depend on the strain. This constitutive, very simple assumption is somehow supported by a physiological argument suggested by the inner structure of the cardiomyocyte. The cardiac myocyte is approximately 25 μm in diameter and about 100 μm in length. The myocyte is composed of bundles of myofibrils that contain myofilaments. The myofibrils have distinct, repeating microanatomical units, termed sarcomeres, which represent the basic contractile units of the myocyte. A microstructural motivation for keeping γ constant can be understood from Figure 2 where cells activated at different levels of prestretch produce a different force to reach nearly the same activated elongation of the sarcomeres [25]. In other words, a bigger active stress is the control used by externally stretched cells to obtain the same target contracted length. This inner behavior prompts us to adopt a constant γ in the constitutive law (11); we shall check *a posteriori* if the nonlinearity of the material yields by itself the correct active stress–strain feedback at the macroscale. The same argument follows from the very steep stress versus sarcomere length plot reported by Kentish et al (see Figure 4b in [26]).
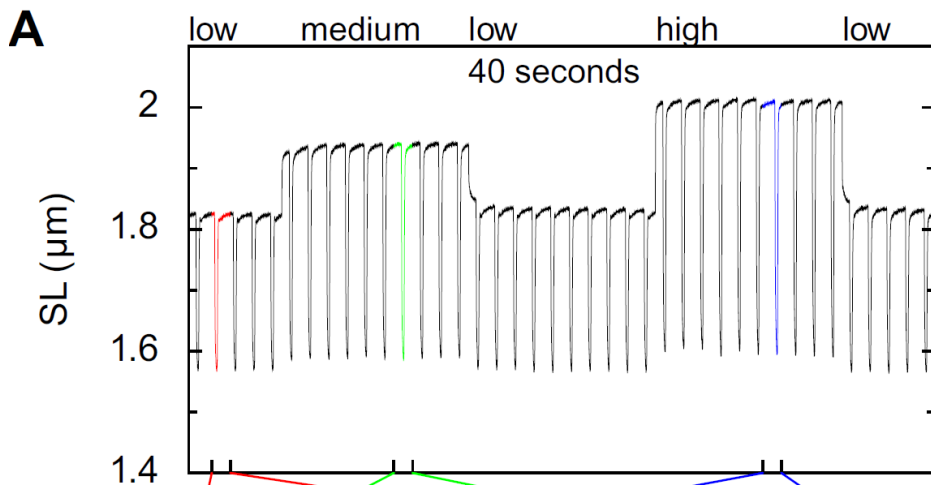
Figure 2. Cells activated at increasing prestretch at the frequency of 1 Hertz produce an increasing force in order to reach nearly the same activated sarcomere shortening (from [25] with permission).

4. GEOMETRY, FIBERS' ARCHITECTURE AND NUMERICAL IMPLEMENTATION

4.1. Geometry and microstructure

All the main modeling and computational difficulties of cardiac mechanics are already present *in nuce* in the numerical simulation of the left ventricular–cavity geometry approximated as a truncated ellipsoid, where the major axis is about two times longer than the minor one.

It is common in the literature to adopt the *prolate coordinate system* to describe the geometry of the ventricle, because it is a convenient starting point to fit patient–specific geometries from medical images [2]. With this curvilinear coordinate system, the position of a point in the space is given by a triplet (λ, μ, θ) as follows:

$$\begin{cases} x = d \sinh \lambda \sin \mu \cos \theta, \\ y = d \sinh \lambda \sin \mu \sin \theta, \\ z = d \cosh \lambda \cos \mu, \end{cases}$$

where d is the *focal length*, $\lambda \geq 0$, $\mu \in [0, \pi)$ and $\theta \in (0, 2\pi]$.
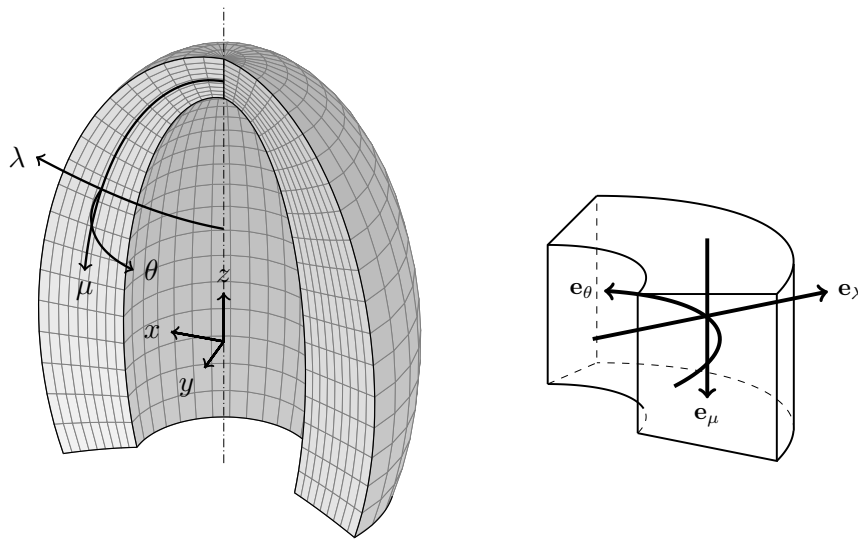
Figure 3. Prolate coordinate system (λ, μ, θ) and the corresponding orthogonal basis $\mathbf{e}_\lambda$, $\mathbf{e}_\mu$ and $\mathbf{e}_\theta$.

The coordinate λ measures the distance of a point from the major axis along a hyperbola (see Figure 3); thus, for a fixed value of λ, the other two variables μ and θ span an ellipsoidal surface with major and minor axes equal to $d \cosh \lambda$ and $d \sinh \lambda$, respectively. The focal length d is a scaling factor and, for the human left ventricle, it ranges between 3.5 and 4.5 cm.

Given the domain

$$\tilde{\Omega}_0 := \left\{ (\lambda, \mu, \theta) \colon \lambda_{\mathsf{endo}} < \lambda < \lambda_{\mathsf{epi}}, \ 0 < \mu < \mu_{\mathsf{base}}, \ 0 \leq \theta < 2\pi \right\}, \tag{12}$$

with parameters taken from [27], we define the computational domain Ω_0 (i.e. the left ventricle) by first translating $\tilde{\Omega}_0$ in order to have the basal endocardium ring at $z = 0$, and then intersecting it with the set $\{z < 0\}$.

The prolate coordinate system is curvilinear, the associated metric tensor is not constant but the local basis of the tangent space $\{\mathbf{e}_\lambda, \mathbf{e}_\mu, \mathbf{e}_\theta\}$ at a given point (λ, μ, θ) is orthogonal. Fibers and sheets direction are defined by means of a linear combination of the normalized basis $\mathbf{e}_{\langle \lambda \rangle}$, $\mathbf{e}_{\langle \mu \rangle}$ and $\mathbf{e}_{\langle \theta \rangle}$ as follows:

$$\begin{aligned} \mathbf{f}_\circ &= \cos \alpha(\lambda_*) \, \mathbf{e}_{\langle \theta \rangle} + \sin \alpha(\lambda_*) \, \mathbf{e}_{\langle \mu \rangle}, \\ \mathbf{s}_\circ &= \sin \beta(\lambda_*) \Big(\sin \alpha(\lambda_*) \, \mathbf{e}_{\langle \theta \rangle} - \cos \alpha(\lambda_*) \, \mathbf{e}_{\langle \mu \rangle} \Big) + \cos \beta(\lambda_*) \, \mathbf{e}_{\langle \lambda \rangle}, \end{aligned} \tag{13}$$

8

with $\alpha(\lambda_*) = \alpha_{\mathsf{endo}}(1 - \lambda_*) + \alpha_{\mathsf{epi}} \lambda_*$ and $\beta(\lambda_*) = \beta_{\mathsf{endo}}(1 - \lambda_*) + \beta_{\mathsf{epi}} \lambda_*$. The parameter $\lambda_* \in [0, 1]$ measures the wall depth: $\lambda_* = 0$ refers to the endocardium while $\lambda_* = 1$ identifies the epicardium, according to the following definition

$$\lambda_* := \frac{\lambda - \lambda_{\mathsf{endo}}}{\lambda_{\mathsf{epi}} - \lambda_{\mathsf{endo}}}.$$

It is easy to check that, by definition (13), fibers and sheets are everywhere orthogonal. This property is required by constitutive mechanical reasons because, as showed in Section 2, the symmetry group of an orthotropic material is defined through an orthonormal basis $\{\mathbf{f}_\circ, \mathbf{s}_\circ, \mathbf{n}_\circ\}$.

The orientation of the cardiac fibres according to this protypical law neglects the the mechanical impact of more complex but more physiological distributions. In particular, non null imbrication angle, non-symmetric and non-linear transmural variation of the helix angle are not accounted for in the present work. This choice is made on purpose, to keep the parametrization of the geometrical model at a minimum degree of complexity.

4.2. Numerical approximation of the PV-loop

In the heart, the systole starts when the electric potential triggers the sarcomeres twitch inside the myocytes. This marks the end–diastolic point (EDP) of the PV-loop, just after that the blood has been pushed by the atrial contraction and ventricle relaxation inside the ventricle itself through the mitral valve. The contraction of the fibers suddenly increases the cavity pressure, the mitral valve closes and the ventricle undergoes an *isovolumic* strain: the incompressibility of blood preserves the chamber volume during the twitch. During this phase the inner pressure significantly raises from the end–diastolic value (which is the *preload*) to the arterial one (*afterload*), reached when the aortic valve opens.

Let $\mathcal{V}_{\mathsf{inner}}(\varphi)$ be the inner volume computed from the deformation φ. During the isovolumic contraction, the following constraint has to be variationally imposed:

$$\mathcal{V}_{\mathsf{inner}}(\varphi) = V_{\mathsf{EDP}},$$

where V_{EDP} is the constant end–diastolic volume. The corresponding Lagrange formulation reads:

$$\mathscr{L}(\varphi, p, p_{\mathsf{inner}}; \gamma, V_{\mathsf{EDP}}) := \int_{\Omega_0} \mathcal{W}\big(\mathsf{F}(\varphi)\mathsf{F}_{\mathsf{a}}^{-1}(\gamma)\big) \, \mathrm{d}V - \int_{\Omega_0} p\,(J - 1) \, \mathrm{d}V \\ - p_{\mathsf{inner}} \big(\mathcal{V}_{\mathsf{inner}}(\varphi) - V_{\mathsf{EDP}}\big), \tag{14}$$

where the first integral is the strain–energy, while the second accounts for the incompressibility of the material. To enforce the preservation of the inner volume, the (scalar) Lagrange multiplier p_{inner} has been introduced. Finally, the activation $\gamma = \gamma(t)$ is prescribed at the (fictitious) time t.

The volume $\mathcal{V}_{\mathsf{inner}}(\varphi)$ can be calculated by a surface integral

$$\mathcal{V}_{\mathsf{inner}}(\varphi) = \int_{\varphi(\Omega_{\mathsf{inner}})} \mathrm{d}v = \frac{1}{3} \int_{\partial\varphi(\Omega_{\mathsf{inner}})} \mathbf{x} \cdot \mathbf{n} \, \mathrm{d}a = -\frac{1}{3} \int_{\partial\varphi(\Gamma_{\mathsf{endo}})} \mathbf{x} \cdot \mathbf{n} \, \mathrm{d}a,$$

where Ω_{inner} is the volume enclosed by the endocardium Γ_{endo} and the plane at $z = 0$, and $\mathbf{n}$ is the outgoing unit normal vector.

The saddle–point of the functional (14) can be characterised taking the first variation of $\mathscr{L}$ in $(\varphi, p, p_{\mathsf{inner}})$:

$$\begin{cases} \langle \mathrm{D}_{\varphi}\mathscr{L}, \boldsymbol{\eta} \rangle = \int_{\Omega_0} \big(\mathsf{P}(\mathsf{F}\mathsf{F}_{\mathsf{a}}^{-1})\mathsf{F}_{\mathsf{a}}^{-\mathsf{T}} - p\operatorname{cof}\mathsf{F}\big) : \operatorname{GRAD}\boldsymbol{\eta} \, \mathrm{d}V - p_{\mathsf{inner}} \int_{\Omega_0} \mathrm{D}_{\varphi}\mathcal{V}_{\mathsf{inner}} \cdot \boldsymbol{\eta} \, \mathrm{d}V = 0, \\[2mm] \langle \mathrm{D}_p\mathscr{L}, q \rangle = -\int_{\Omega_0} q\,(J - 1) \, \mathrm{d}V = 0, \\[2mm] \langle \mathrm{D}_{\xi}\mathscr{L}, q_{\mathsf{inner}} \rangle = -q_{\mathsf{inner}} \big(\mathcal{V}_{\mathsf{inner}} - V_{\mathsf{EDP}}\big) = 0, \end{cases} \tag{15}$$

for all $(\boldsymbol{\eta}, q, q_{\text{inner}}) \in V \times Q \times \mathbb{R}$, with $V \subseteq \mathcal{T}_{\boldsymbol{\varphi}}\mathscr{C}$ and $Q = \mathrm{L}^2(\Omega_0)$.

The derivative $\mathrm{D}_{\boldsymbol{\varphi}}\mathcal{V}_{\text{inner}}$ can be explicitly calculated as follows:

$$\langle \mathrm{D}_{\boldsymbol{\varphi}}\mathcal{V}_{\text{inner}}, \boldsymbol{\eta} \rangle = \int_{\Omega_{\text{inner}}} \mathrm{cof}\,\mathsf{F} : \mathrm{GRAD}\,\boldsymbol{\eta}\,\mathrm{d}V = -\int_{\partial\boldsymbol{\varphi}(\Gamma_{\text{endo}})} (\boldsymbol{\eta} \circ \boldsymbol{\varphi}) \cdot \mathbf{n}\,\mathrm{d}a.$$

We observe that p_{inner} is nothing but the (unknown) inner pressure, to be applied in order to have the inner volume equal to V_{EDP} (given).

From an implementation viewpoint, the Newton-Raphson method applied to a finite elasticity problem (15) rewrites in solving a linearized and then discretized problem where the second order derivative of the Lagrangian is symmetric (although not positive definite since it is a saddle-point problem); this can be exploited in the numerical solution of the linear system (for instance by a Cholesky decomposition).

In absence of commonly accepted physiological boundary conditions at the base and at the epicardium, we fix the normal displacement of the base have fixed normal (axial) displacement $\Gamma_{\text{base}} = \overline{\Omega}_0 \cap \{z = 0\}$. Then we adopt the weakest possible choice that mathematically ensure well posedness: null average displacement and null average rotation of the ventricle. The actual implementation of these constraints rewrites in terms of two conditions to be appended to the Lagrange functional with three scalar multipliers to be determined (see details in [16]).

The constant–volume contraction ends when the inner pressure is high enough to open the aortic valve and let the blood flow outside. This stage is called *ejection phase*, and it is located in the P–V curve between the aortic valve opening (AVO) and the aortic valve closing (AVC).

During the ejection phase, pressure and volume in the chamber are related in a complex manner, since the time–variation of the volume depends on the valve geometry, on the compliance of the arterial vessels, on the overall resistance of the circulatory system, and so on. It is not the purpose of the present work to address such issues not even partially, so we simply fix an end–systolic pressure and compute the volume from the corresponding deformation, moving along a horizontal line in the P–V plane.

The only computational issue for this branch of the PV-loop is the valve opening effect to be encoded in the mechanical model. During the isovolumic contraction, the pressure is a Lagrange multiplier that can be controlled through the activation parameter γ, i.e. a function $\gamma \mapsto p_{\text{inner}}(\gamma)$. The afterload pressure $p_{\text{afterload}}$ is targeted according to the following strategy: γ is increased step by step and when the threshold is crossed, we apply a root–finding algorithm (the Brent's method, in our case) to the equation $p_{\text{inner}}(\gamma) = p_{\text{afterload}}$, for γ between the last two computed values. In general, after less than six iteration the Newton residual is below the requested tolerance (10^{-8}).

The diastolic phase resembles the systole from the implementation viewpoint: when γ reaches its maximum value, the aortic valve is closed, and so the isovolumic relaxation starts. The deactivation continues until the inner pressure is below the preload p_{preload}, when the mitral valve opens. The last phase closes the loop by keeping the pressure constant.

5. RESULTS AND DISCUSSION

The simulations illustrated in this section start with a passive inflation up to the end–diastolic pressure $p_{\text{preload}} = 1$ kPa. Then, an entire PV–loop is approximated by a linear increase of γ up to 0.2 and $p_{\text{afterload}} = 10$ kPa, and backward. The value $\gamma = 0.2$ is fixed on the basis of best fit of experiments with sheets of active cardiomyocytes [16].

The stages of the PV-loop are graphically illustrated in Figure 4 with the table of fixed corner values. For the canine geometry, the stroke volume, defined as the difference between the end–diastolic and end–systolic volumes, is about 22.56 ml, which yields an ejection fraction (the stroke volume over the end–diastolic volume) of 56%. This value is within the physiological range for a normal heart.

Numerical simulations are performed with different combinations of material parameters and microstructure. Our reference set up of parameters involves a radial sheet distribution, a symmetric $\pm 60°$ fiber orientation across the wall and material parameters from [8].
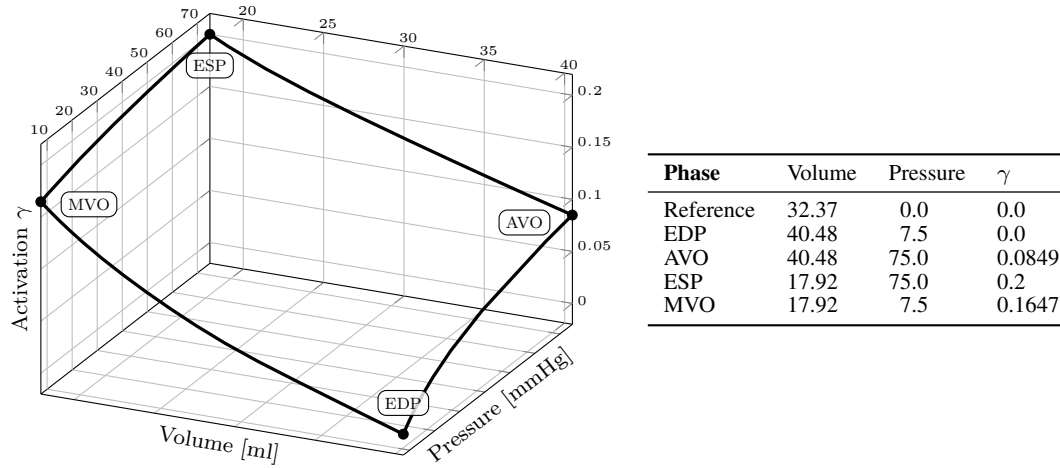
Figure 4. Pressure, volume and contraction at key points of the PV–loop, namely end–diastolic point (EDP), aortic valve opening (AVO), end–systolic point (ESP) and mitral valve opening (MVO). The reference configuration is initially passively inflated to reach the end–diastolic point. Note that the contraction parameter γ does not vanish at MVO, but at EDP.

Phase	Volume	Pressure	γ
Reference	32.37	0.0	0.0
EDP	40.48	7.5	0.0
AVO	40.48	75.0	0.0849
ESP	17.92	75.0	0.2
MVO	17.92	7.5	0.1647

Results of the numerical simulations are post–processed to evaluate the ability of the mathematical model to reproduce relevant physiological quantities: thickening, total length of the ventricle, stroke volume, transmural strain and stress, torsion. According to [28], there is no standard protocol to measure the torsion of the left ventricle, and two formulas are reported as most significant:

$$\sin \tau_{\theta\mu}^1 = \frac{2\mathsf{E}_{\theta\mu}}{\sqrt{1 + 2\mathsf{E}_{\theta\theta}}\sqrt{1 + 2\mathsf{E}_{\mu\mu}}}, \qquad \text{(case 1)}$$

$$\tau_{\theta\mu}^2 = \frac{\phi_{\mathsf{base}}r_{\mathsf{base}} - \phi_{\mathsf{apex}}r_{\mathsf{apex}}}{D}. \qquad \text{(case 2)}$$

The first formula relies on the Green tensor E and is therefore intrinsically objective, while the second one deserves more explanations. Given two axial sections of the ventricle, one near the base and the other just above the apex, separated by a distance D, we select one point per section, say $\mathbf{X}_{\mathsf{base}}$ and $\mathbf{X}_{\mathsf{apex}}$, initially aligned. The deformation maps these two points to $\mathbf{x}_{\mathsf{base}}$ and $\mathbf{x}_{\mathsf{apex}}$, respectively. Then we compute

$$R = \|\mathbf{X} - (\mathbf{X} \cdot \mathbf{e}_3)\mathbf{X}\|, \quad r = \|\mathbf{x} - (\mathbf{x} \cdot \mathbf{e}_3)\mathbf{x}\|, \quad \sin\phi = \frac{\mathbf{x} \wedge \mathbf{X} \cdot \mathbf{e}_3}{rR},$$

for both sections, and eventually the torsion $\tau_{\theta\mu}^2$.

In Figures 5 and 6 are plotted several relevant mechanical fields computed during a cardiac cycle. The simulation starts at the end of the passive filling stage, during which the venous pressure raises the inner volume from 32 to about 40 ml. In the following we compare these results with statistically significant normal human values [29]. Reference length ratios are taken using values at systole and diastole (and not vs. the relaxed configuration), the only possible protocol that can be adopted *in vivo*.

During the systolic phase, the difference in peak radial displacement between endocardium and epicardium (Figure 6) tells us that the wall thickens for 36%, while the ventricle shortens of about 4% (not shown). These values are slightly smaller than the physiological ones. Under the incompressibility constraint, the transmural orientation of the fibers favors the transverse shear, and then thickening, with respect to axial elongation [30, 28].

The strain distribution across the wall (Figure 5) is within the physiological range [31]. The hoop strain is around -20% at the sub–endocardium and -2% at the sub–epicardium, which
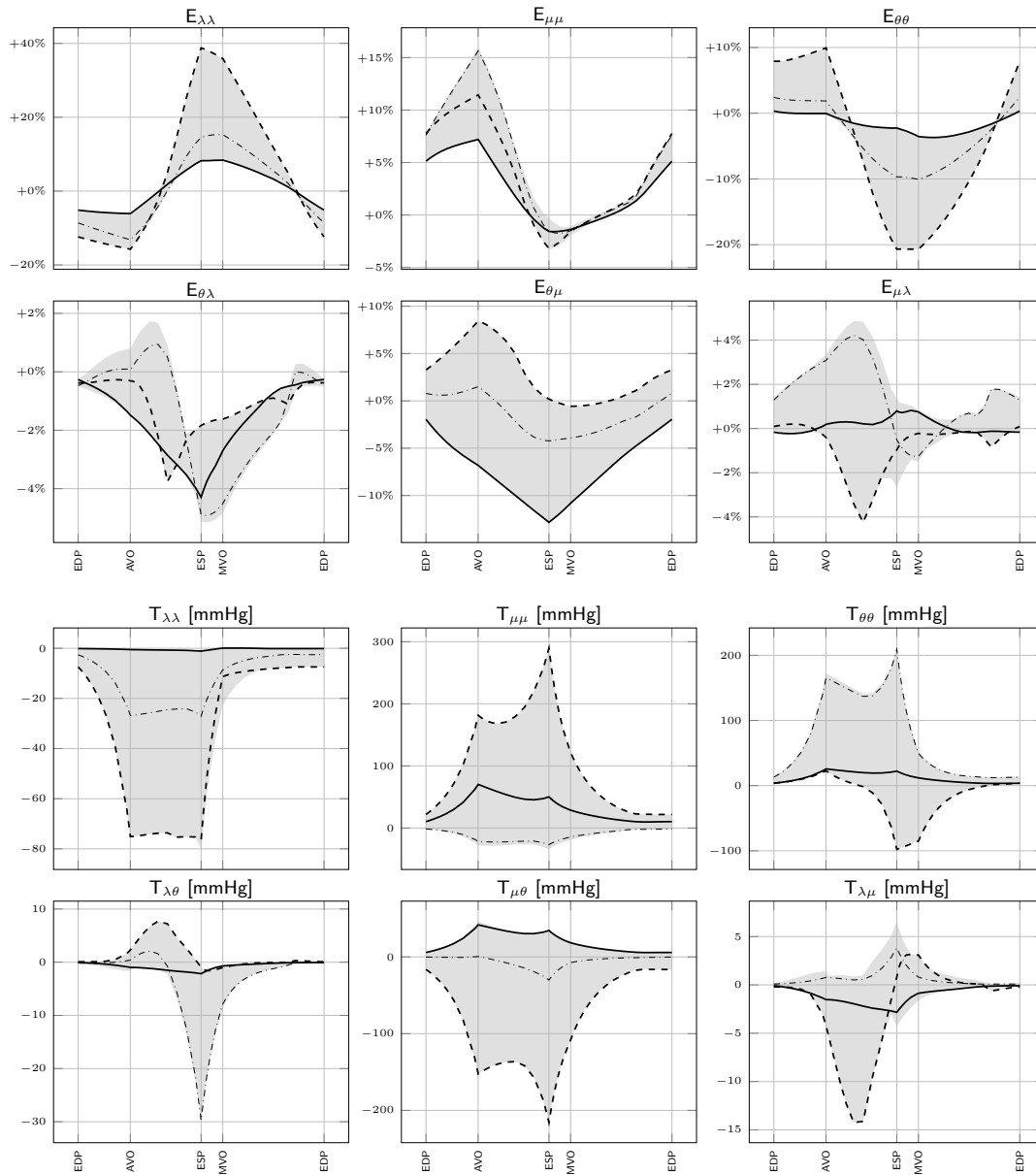
Figure 5. Plot of the Green-Lagrange strain (upper) and Cauchy stress (lower) components during the cardiac cycle of a canine ventricle. The data refer to a mid-axis section of the ellipsoid. At a given time, the shaded area represents the range of values transmurally spanned by the specific field in the radial direction. The lines refer to the sub–epicardium (solid line), sub–endocardium (dashed line), and mid–myocardium (dash–dotted line). The time (abscissa) is fictitious, so no scale is provided.

yields a significantly higher transmural variation than the strain in the fibers direction (the latter being gathered from $\mathcal{I}_{4,\mathbf{f}_\circ}$). We conjecture that this could be physiologically advantageous from a structural point of view: myocytes bear nearly the same mechanical load *irrespective* of the transmural position.

Among the off–diagonal components of the strain, $E_{\theta\mu}$ takes the largest values (the same occurs for the Cauchy stress T). This is not surprising since the longitudinal–circumferential shear is associated to the torsion (and it is indeed exploited to compute the torsion with the formula (case 1)).
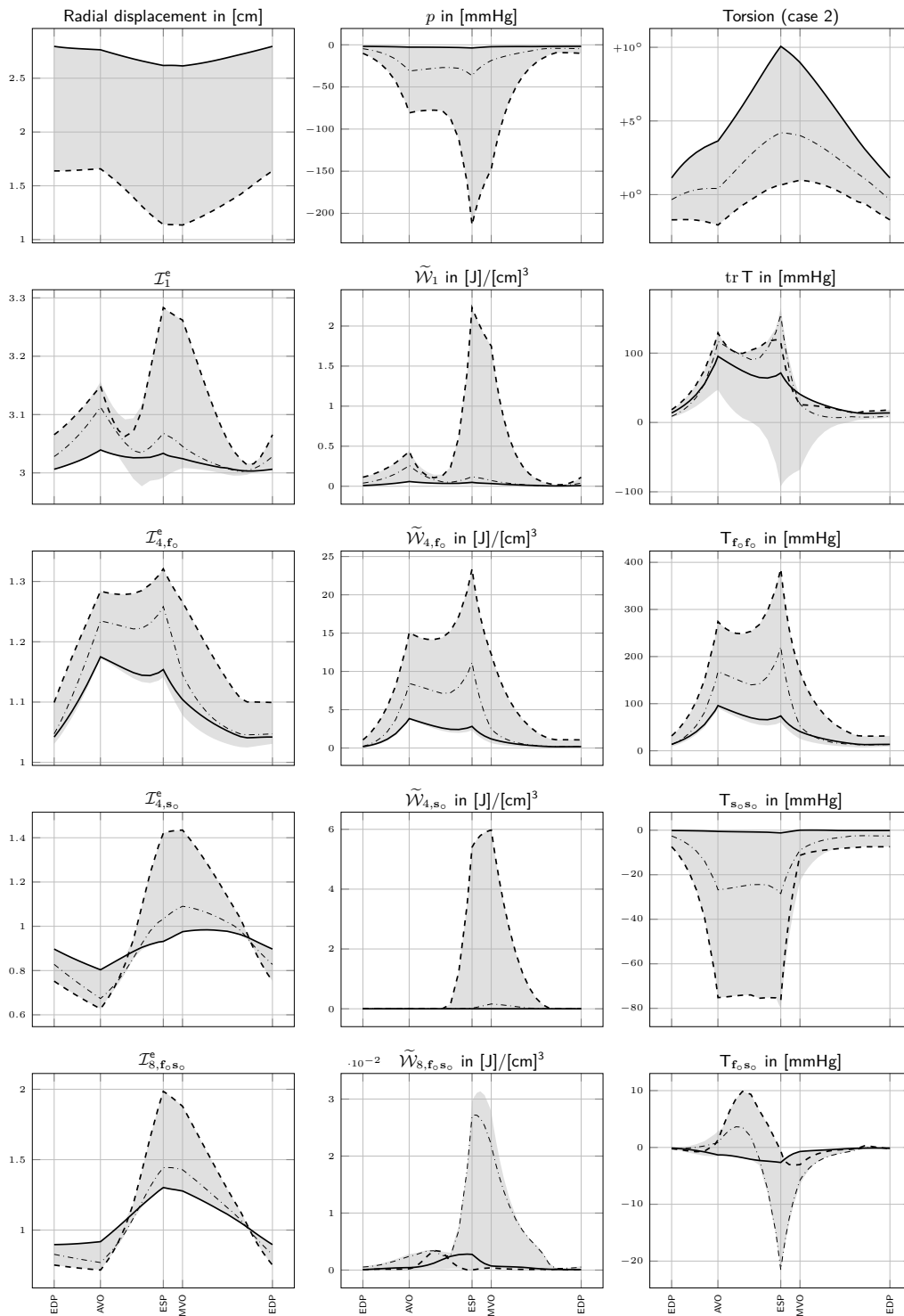
Figure 6. Plot of radial displacement, pressure, strain invariants based on $\mathsf{F_e}$, components of the strain–energy density and stress, during the cardiac cycle. The strain invariants do not account for the visible strain (reported in Figure 7) but they dictate the stored strain energy. Notice that $\mathcal{I}^{\mathrm{e}}_{4,\mathbf{f}_\circ}$ is always positive. The data refer to a mid-axis section of the ellipsoid. At a given time, the shaded area represents the range of values transmurally spanned by the specific field in the radial direction. The lines refer to the sub–epicardium (solid line), sub–endocardium (dashed line), and mid–myocardium (dash–dotted line). The time (abscissa) is fictitious, so no scale is provided.
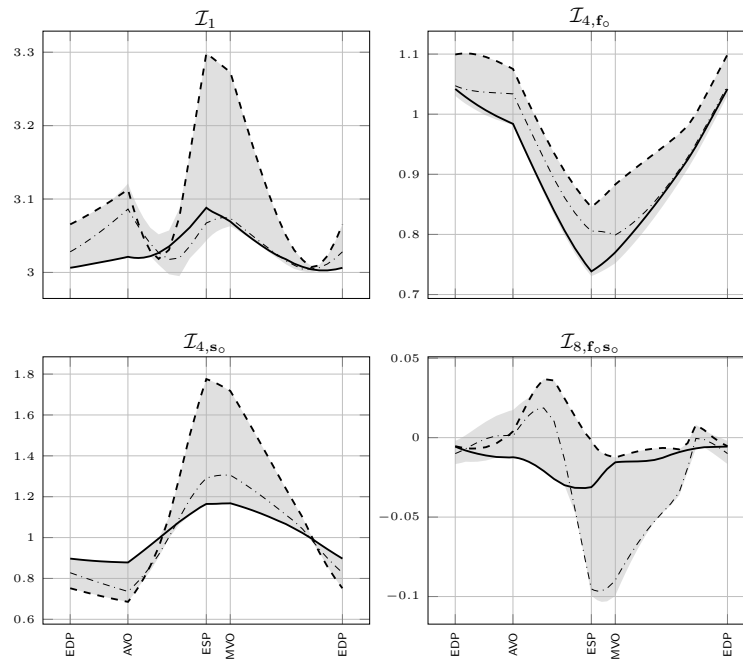
Figure 7. Plot of the strain invariants calculated on the basis of the apparent deformation F, during the cardiac cycle. The data refer to a mid-axis section of the ellipsoid. At a given time, the shaded area represents the range of values transmurally spanned by the specific field in the radial direction. The lines refer to the sub–epicardium (solid line), sub–endocardium (dashed line), and mid–myocardium (dash–dotted line). The time (abscissa) is fictitious, so no scale is provided.

All the components of the stress exhibit a peak at end systole, a signature of the exponential form of the strain energy which manifests itself at large (microstructural) strains.

The value of the transmural pressure is of the same order of magnitude as the biggest component of the Cauchy stress: therefore p contributes as much as the strain energy to the principal components of the stress. An accurate enforcement of the incompressibility constraint is therefore essential to compute the stress field correctly; in our computations $|\det \mathsf{F} - 1| < 10^{-8}\ \forall \mathbf{X}$.

5.1. Axial torsion and transverse shear

Two shear deformations can be identified: a rotation of the apex with respect to the base (say *axial* torsion) and a rotation of the endocardium with respect to the epicardium (*transmural* shear). They are both associated to the shear stress, $\mathsf{T}_{\theta\mu}$ and $\mathsf{T}_{\theta\lambda}$, respectively, that are generated by the asymmetric distribution of the fibers; the shortening of the left handed epicardial fibers induces a rotation opposite to the one of the right handed endocardial ones. The force balance is generally in favor of the epicardial fibers because of the longer arm of their torque. Torsion is therefore essentially dictated by the mechanical functionality of the fibers.

We calculate a significant longitudinal torsion of the ventricle during the contraction (Figure 6). The difference between diastole and systole at epicardium is about $15°$, a value consistent with the physiological range [32]. The plot of torsion versus time computed using the two formulas are quite similar, the maximum value obtained using the formula (case 1) being slightly higher.

A significant transmural shear is observed during the cardiac cycle (see Figure 8). At systole we numerically find that near the base the endocardium slightly rotates clockwise (view from the apex of the ventricle) and the epicardium rotates counterclockwise, while the opposite occurs during relaxation. This transmural shear is also apparent, at minor extent, when the ventricle isovolumically contracts, in the early systolic phase. The shear is not homogeneous along the longitudinal direction: moving towards the apex, it changes sign around $\mu = \frac{\pi}{2}$, so that the rotation is in the opposite

End diastole

Aortic valve opening

End systole

Mitral valve opening
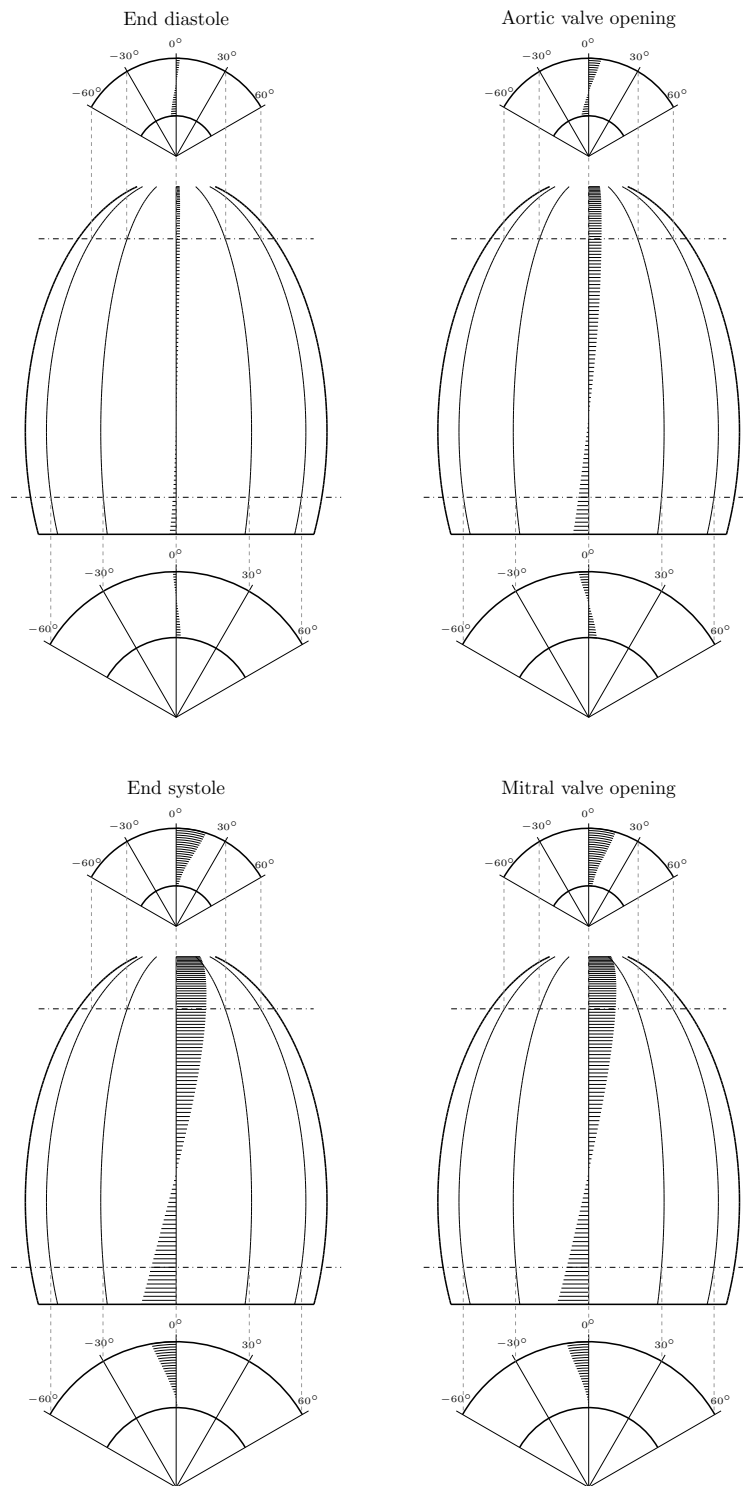
Figure 8. Torsion of the ventricle at four stages of the PV-loop. The mid-figure strip refers to the epicardium, while top and bottom figures represent the in-plane transversal rotation at the base and the apex, respectively. The epicardial torsion (difference in the rotation angle) at end diastole is very small, it is appreciable at the aortic valve opening and, as expected, it reaches its maximum during the ejection phase. The in-plane transversal shear reflects a rotation in opposite directions of the inner and external walls at the AVO, while during the ejection the epicardium only rotates for a large angle, the rotation of the endocardium being very small.

direction near the apex (which yields a different longitudinal torsion at the sub–endocardium and the sub–epicardium). In the midsection and near the apex the shear is positive, meaning that the epicardium rotates counterclockwise while the endocardium clockwise, and it ranges from 0.02 at the diastole to 0.14 at the systole.

The transverse shear resulting in our numerical simulations is also reported in the physiological literature [33, 28] (see Figure 9), but with an important difference: the internal and external rotation in a given axial plane are observed to occur in the *same* direction with a *decreasing* amplitude going from the internal to the external boundary. This behavior is paradoxical on the basis of our mechanical understanding, since the rotation is expected to be dictated by the fibers on the epicardium, which take advantage of their longer arm; therefore we coherently predict a larger epicardial rotation that can, at most, contrast the rotation of the endocardial surface in its (opposite) direction.
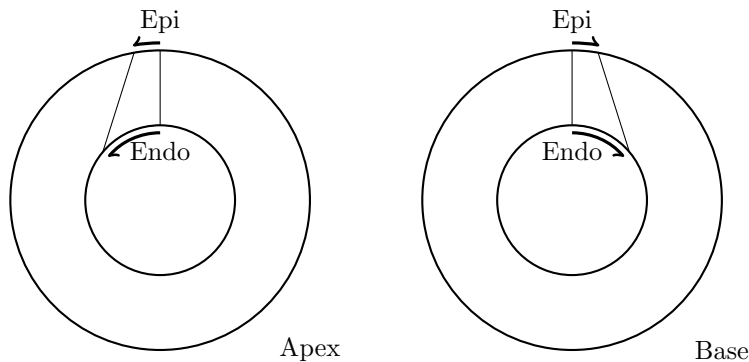
Figure 9. Physiological rotation of the endo and epicardium occur in the same direction, the inner being larger than the outer one. This behavior (not numerically reproduced) is paradoxical on the basis of our current understanding of cardiac mechanics and not yet understood.

To get rid of such a puzzle, we observe that sheets are radially oriented, while fibers are in circumferential layers, so that the transverse shear is measured by the eighth invariant $\mathcal{I}_{8,\mathbf{f}_\circ \mathbf{s}_\circ}$. As it is well known that it is difficult to evaluate experimentally the shear moduli of soft biological tissues, we have conjectured that a greater stiffness modulus in the corresponding strain–energy term might affect the results discussed above. As a matter of fact, we do not notice significant modifications in the results when the shear modulus a_{fs} is 5 times greater (not shown).

In our opinion the failure of the numerical model in reproducing the experimentally observed transverse rotation goes beyond a mere tuning of the parameters: there is some deeper mechanism which is still to be understood together with its encoding in terms of mathematical equations (see a nice discussion in [28] in this respect). We just mention that according to [33] the transverse fiber angle (or *imbrication* angle) is responsible for the mechanical paradox illustrated above. We do not address this possible explanation in the present work, where fibers always lie on surfaces at constant λ.

5.2. Energy partition

If the orientation of the fibers across the wall spans an interval smaller than the commonly accepted one $(-60^\circ, 60^\circ)$, the isovolumic contraction exhibits an unphysiological elongation of the ventricle (not shown). Conversely, with a standard distribution of fibers, the apparent deformation F is small, as certified by the nearly constant value of $\mathcal{I}_{4,\mathbf{f}_\circ}$ calculated between the EDP and the AVO stages (see Figure 7).

This observation suggests an energetic argument to interpret the optimality of the fibers architecture in the cardiac tissue [34]. If the fibers are physiologically oriented, they do not produce apparent strain during the isovolumic contraction, as they are *designed* to produce, at this stage, the maximum compression of the inner blood volume. Energy possibly spent during the isovolumic

branch of the PV–loop to give rise to visible displacement would be wasted; so we can argue that the fiber architecture is designed to maximize the incompatibility of F_a and make $F \simeq I$. The strain energy $\mathcal{W} \simeq \mathcal{W}(F_a^{-1})$ storage is here maximized to provide the maximum stroke volume in the ejection phase that follows, by using also the simple passive relaxation of the (not any more activated) elastic walls.

As expected, the largest contribution in the strain energy comes from $\mathcal{W}_{4,\mathbf{f}_o}$ (Figure 6), while the cardiac material is largely under compression in the fibers' direction during systole, as certified by the value $\mathcal{I}_{4,\mathbf{f}_o} < 1$. Intriguingly, while $\mathcal{I}_{4,\mathbf{f}_o} = F\mathbf{f}_o \cdot F\mathbf{f}_o$ is smaller than one, the strain energy contribution is not turned off, seemingly in contrast with the prescription of vanishing stress contribution of the fibres under compression. As a matter of fact, this is not in contradiction with the form of the Cauchy stress tensor (9) and the discussion at the end of Section 2, because it is calculated from the activated configuration $F_e\mathbf{f}_o \cdot F_e\mathbf{f}_o$, not on the basis of the physical one (Figure 6). This transparent result arises in an active strain framework only.

The sheet–specific contribution encoded in the strain energy $\mathcal{W}_{4,\mathbf{s}_o}$ shows up only in the late systole and early diastole (Figure 6), thus confirming that sheets work in compressive regime during inflation; during the contraction, the thickening and torsion become large enough to compensate the sheets' shortening due to the compression.

The energetic contribution $\mathcal{W}_{8,\mathbf{f}_o\mathbf{s}_o}$ is much smaller than fibers' one $\mathcal{W}_{4,\mathbf{f}_o}$, but comparable or larger than the isotropic one $\mathcal{W}_1$. The eighth invariant $\mathcal{I}_{8,\mathbf{f}_o\mathbf{s}_o}$ is significantly different from zero during the cycle and its value can be interpreted as a measure of the shear strain driven by the twisted contraction of endocardial and epicardial fibers. However, we have seen that removing such a term, no substantial difference arises in terms of volume, torsion, radii and height. On the other hand, the stress distribution is slightly different in all the components, especially the trace of the Cauchy stress and its component along the fibers. This observation is supported by the small contribution to the strain energy provided by $\mathcal{W}_{8,\mathbf{f}_o\mathbf{s}_o}$ (Figure 6). To make this result more robust, we recall that an high uncertainty is known to affect the shear experiments on soft biological tissues [35]. As a matter of fact, such a small energetic contribution of the shear strain in the elastic energy persists under variation of the corresponding elastic modulus for an order of magnitude (not shown). The minor relevance of the sheets architecture in the cardiac dynamics (with fixed material parameters) is confirmed by the sensitivity analysis reported in Figure 10: at variance of the orientation of the sheets there is no significant modification in the indicators of the cardiac activity.

These observations support the conclusion that the Holzapfel–Ogden model effectively accounts for the laminar structure of the myocardium that is at some extent relevant in the systole. On the other hand, for the material parameters reported in the literature, the contribution of the sheets is secondary with respect to the one of fibers structure.

5.3. End systolic pressure raise vs. end diastolic pressure

The stroke volume of the heart linearly increases in response to an increase in the end diastolic volume, a self–regulation mechanism known as Frank–Starling law [36]. In tissue–scale mathematical models it is usually represented in terms of a stretch–dependent active stress, introducing further complexity (and a possible source of instability) in the mechanical model. There is a common agreement that the subcellular explanation of this adaptation of the produced stress to pre–stretch of the muscle is the increased Calcium sensitivity [26].

In our model we do not explicitly encode any subcellular dynamics; the factor γ here enforces at a macroscopic level the shortening of the fibers and it is taken independent of the stress state of the body. Therefore there can be no expectations about the possibility to reproduce behaviors based on unresolved subcellular electrophysiology. However, it is worth to mention that in an active strain framework an increase in the preload is naturally accompanied by an even higher increase in the end–systolic pressure. We have performed several simulations passively inflating the ventricle up to a given pressure, and then triggering an isovolumic contraction with $\gamma = 0.1$. The result plotted in Figure 11 clearly shows that the end–systolic pressure grows nonlinearly with the preload.

An elementary explanation of this behavior can be understood considering a lumped system composed by an activable spring of stiffness κ and subject to a force f_0. The spring is initially
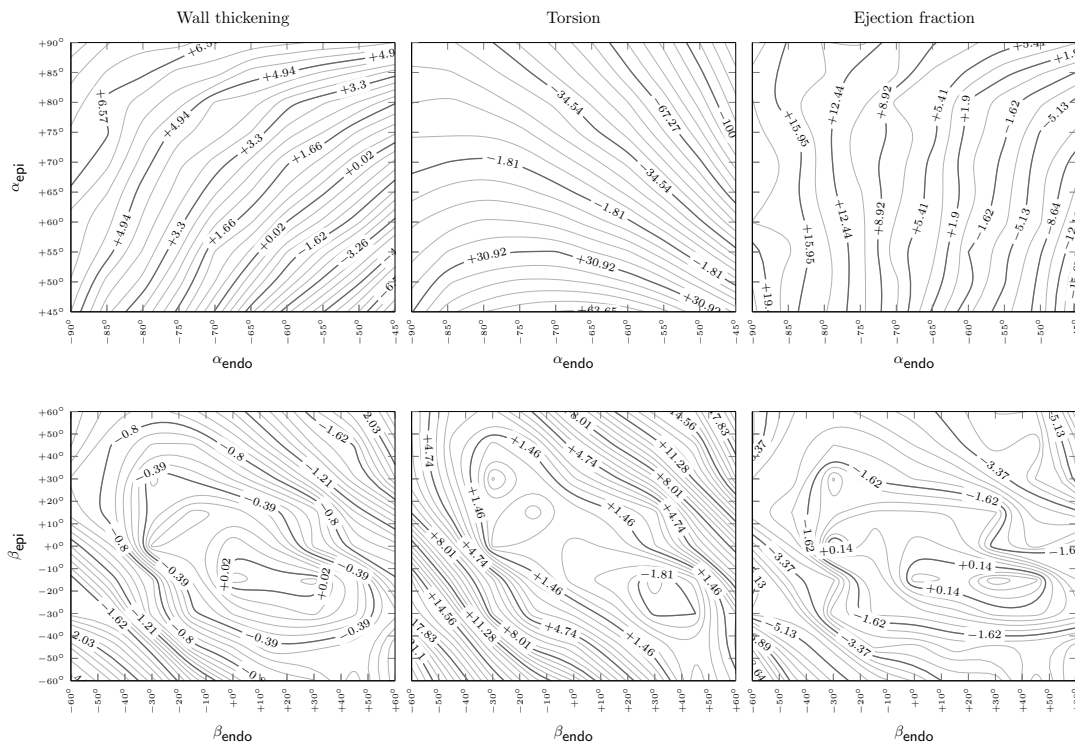
Figure 10. Sensitivity of the computed thickening, torsion end ejection fraction with respect to the fibers and sheets angle (α and β in (13)). The relative discrepancy of between the computed solution and the reference one (radial sheets and $\pm 60°$ fibers) is plotted in the plane of the endocardium and epicardium angles.
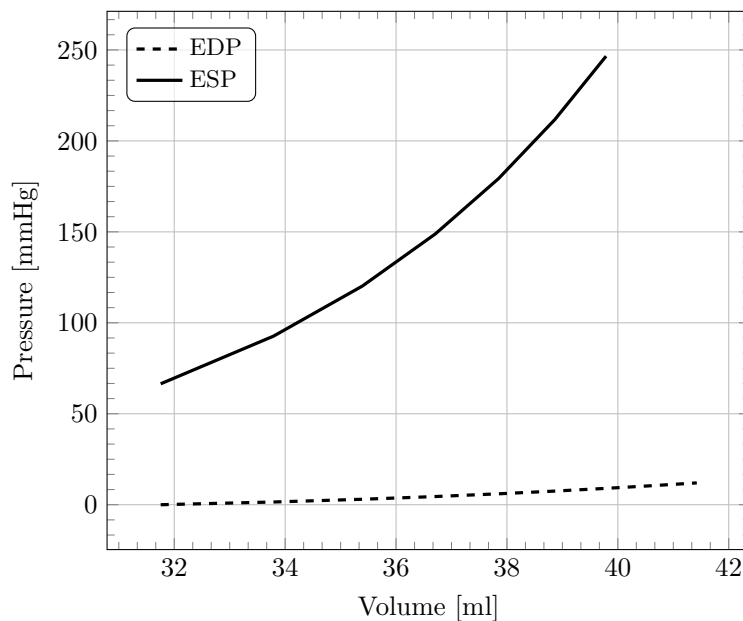
Figure 11. End–systolic pressure dependency on end–diastolic pressure. At a given value of EDP (dashed line), during isochoric contraction the cardiac muscle produces the pressure that can be found on the ESP line (bold line) for fixed volume.

not activated and the corresponding elongation x_0 satisfies

$$\kappa x_0 = f_0.$$

If the elongation is fixed at x_0 and then the spring is activated, the reference strain passes from 1 to x_a, and the corresponding produced force f is

$$f = \kappa x_0 / x_\mathsf{a}.$$

It follows that the actively produced force at fixed apparent elongation x_0 grows linearly with the prestress f_0.

This elementary argument makes transparent the reason why in an active strain framework the ESP grows with EDP in such a natural way: the ventricle prefill volume, represented by x_0, is recorded in the passive stress f_0 that dictates the magnitude of the active stress f and raises the blood pressure. While this argument is manifestly too simple to account for the real subcellular physiology of the system, it intriguingly captures some qualitative behavior.

FINAL REMARKS

In this paper we have discussed a numerical simulation of the cardiac cycle in a prolate ellipsoid using an active strain formulation of the Holzapfel–Ogden strain energy. The finite elements computation has been carried on an unstructured (tetrahedral) grid, using a two–fields formulation of the equations and mixed (quadratic–linear) conformal basis. The solution of the discrete nonlinear problem is achieved by a Newton–Raphson scheme.

- The numerical scheme is robust and, in the wide range of parameters explored, it never exhibits instabilities. The Newton–Raphson method converges rapidly, provided that the pseudo-time step is sufficiently small. About $8\,000$ quadratic finite elements, yielding 9 degrees of freedom across the wall thickness, are sufficient to capture an accurate deformation and stress field.
- The very weak boundary conditions adopted perform well from a numerical point of view, enforcing null average displacement and rotation without introducing further hand–tuned boundary conditions.
- The predicted passive filling during diastole, the stroke volume, elongation of the height, strain and torsion are in the range of physiological values. Cardiac wall thickening and axial elongation in systole are slightly below the physiological ones.
- Numerical results are weakly sensitive to the material parameters in the variability range spanned by different papers. Sheets play a minor role in the overall strain energy (for fixed material moduli) while a strong dependence on the fibers orientation has been observed. The contribution of the $\mathcal{I}_{8,\mathbf{f}_\circ \mathbf{s}_\circ}$ invariant is negligible.
- We find that the contribution of the pressure in the stress is as large as the one due to the strain–energy, and incompressibility dictates the torsion. Results highlight that an accurate numerical implementation of the incompressibility constraint is mandatory.
- In our active strain setting, the stress term depending on the fibers' deformation $\widetilde{\mathcal{W}}_{4,\mathbf{s}_\circ}$ is not turned off for stability reasons under compression, because it depends on the fourth invariant $\mathcal{I}_{4,\mathbf{s}_\circ}^{\mathsf{e}}$ calculated from $\mathsf{F}_\mathbf{e}$, and it is always bigger than one in our computations. Interstingly, this is in agreement with recent works on the mechanical role of fibres in muscles [37].
- The pressure jump generated by the active contraction in the isochoric phase grows vs. the prestretch dictated by the volume prefill, even though the contraction length of the microstructure γ is kept constant, independent of the macroscopic strain. This seem a natural framework where quantitative modelling of the coupling between cell level electrophysiology and macroscopic stress could be addressed in the future.

REFERENCES

1. Streeter DD, Spotnitz HM, Patel DP, Ross J, Sonnenblick EH. Fiber orientation in the canine left ventricle during diastole and systole. *Circulation research* 1969; **24**(3):339–347.
2. LeGrice I, Hunter P, Young A, Smaill B. The architecture of the heart: a data–based model. *Philosophical Transactions of the Royal Society of London. Series A: Mathematical, Physical and Engineering Sciences* 2001; **359**(1783):1217–1232.
3. Humphrey J, Yin F. On constitutive relations and finite deformations of passive cardiac tissue: I. a pseudostrain-energy function. *Journal of biomechanical engineering* 1987; **109**(4):298–304.
4. Guccione J, McCulloch A, Waldman L. Passive material properties of intact ventricular myocardium determined from a cylindrical model. *Journal of biomechanical engineering* 1991; **113**(1):42–55.
5. Costa KD, Holmes JW, McCulloch AD. Modelling cardiac mechanical properties in three dimensions. *Philosophical transactions of the Royal Society of London. Series A: Mathematical, physical and engineering sciences* 2001; **359**(1783):1233–1250.
6. Holzapfel GA, Ogden RW. Constitutive modelling of passive myocardium: a structurally based framework for material characterization. *Philosophical Transactions of the Royal Society A: Mathematical, Physical and Engineering Sciences* 2009; **367**(1902):3445–3475.
7. Göktepe S, Acharya S, Wong J, Kuhl E. Computational modeling of passive myocardium. *International Journal for Numerical Methods in Biomedical Engineering* 2011; **27**(1):1–12.
8. Wang H, Gao H, Luo X, Berry C, Griffith B, Ogden R, Wang T. Structure-based finite strain modelling of the human left ventricle in diastole. *International journal for numerical methods in biomedical engineering* 2013; **29**(1):83–103.
9. Nobile F, Quarteroni A, Ruiz-Baier R. An active strain electromechanical model for cardiac tissue. *International Journal for Numerical Methods in Biomedical Engineering* 2012; **28**(1):52–71.
10. Rossi S, Ruiz-Baier R, Pavarino LF, Quarteroni A. Orthotropic active strain models for the numerical simulation of cardiac biomechanics. *International Journal for Numerical Methods in Biomedical Engineering* 2012; **28**(6-7):761–788.
11. Eriksson T, Prassl A, Plank G, Holzapfel G. Influence of myocardial fiber/sheet orientations on left ventricular mechanical contraction. *Mathematics and Mechanics of Solids* 2013; **18**(6):592–606.
12. Eriksson T, Prassl A, Plank G, Holzapfel G. Modeling the dispersion in electromechanically coupled myocardium. *International journal for numerical methods in biomedical engineering* 2013; **29**(11):1267–1284.
13. Carapella V, Bordas R, Pathmanathan P, Lohezic M, Schneider JE, Kohl P, Burrage K, Grau V. Quantitative study of the effect of tissue microstructure on contraction in a computational model of rat left ventricle. *PloS one* 2014; **9**(4):e92 792.
14. Baillargeon B, Rebelo N, Fox DD, Taylor RL, Kuhl E. The living heart project: A robust and integrative simulator for human heart function. *European Journal of Mechanics-A/Solids* 2014; .
15. Berberoğlu E, Solmaz HO, Göktepe S. Computational modeling of coupled cardiac electromechanics incorporating cardiac dysfunctions. *European Journal of Mechanics-A/Solids* 2014; .
16. Pezzuto S, Ambrosi D, Quarteroni A. An orthotropic active strain model for the myocardium mechanics and its numerical approximation. *Eur. J. Mech. Solids* 2013; .
17. Hughes TJ, Marsden JE. *Mathematical foundations of elasticity*. Dover Publications, 1994.
18. Antman SS. *Nonlinear problems of elasticity*, vol. 107. Springer, 2005.
19. Bonet J. *Nonlinear continuum mechanics for finite element analysis*. Cambridge university press, 1997.
20. Gurtin ME. *An introduction to continuum mechanics*. Access Online via Elsevier, 1982.
21. Liu IS. On representations of anisotropic invariants. *Int. J. Engng. Sci.* 1982; **20**(10):1099–1109.
22. Merodio J, Ogden R. The influence of the invariant i8 on the stress–deformation and ellipticity characteristics of doubly fiber-reinforced non-linearly elastic solids. *International Journal of Non-Linear Mechanics* 2006; **41**(4):556–563.
23. Nardinocchi P, Teresi L. On the active response of soft living tissues. *Journal of Elasticity* 2007; **88**(1):27–39.
24. Boyett M, Frampton J, Kirby M. The length, width and volume of isolated rat and ferret ventricular myocytes during twitch contractions and changes in osmotic strength. *Experimental physiology* 1991; **76**(2):259–270.
25. Peterson P, Kalda M, Vendelin M. Real-time determination of sarcomere length of a single cardiomyocyte during contraction. *American Journal of Physiology-Cell Physiology* 2013; **304**(6):C519–C531.
26. Kentish JC, Ter Keurs H, Ricciardi L, Bucx J, Noble M. Comparison between the sarcomere length-force relations of intact and skinned trabeculae from rat right ventricle. influence of calcium concentrations on these relations. *Circulation research* 1986; **58**(6):755–768.
27. Guccione JM, Costa KD, McCulloch AD. Finite element stress analysis of left ventricular mechanics in the beating dog heart. *Journal of biomechanics* 1995; **28**(10):1167–1177.
28. Young AA, Cowan BR, *et al.*. Evaluation of left ventricular torsion by cardiovascular magnetic resonance. *Journal of Cardiovascular Magnetic Resonance* 2012; **14**(1):1–10.
29. Dalen H, Thorstensen A, Aase SA, Ingul CB, Torp H, Vatten LJ, Stoylen A. Segmental and global longitudinal strain and strain rate based on echocardiography of 1266 healthy individuals: the hunt study in norway. *European Journal of Echocardiography* 2010; **11**(2):176–183.
30. LeGrice I, Takayama Y, Covell J. Transverse shear along myocardial cleavage planes provides a mechanism for normal systolic wall thickening. *Circulation Research* 1995; **77**(1):182–193.
31. Augustine D, Lewandowski AJ, Lazdam M, Rai A, Francis J, Myerson S, Noble A, Becher H, Neubauer S, Petersen SE, *et al.*. Global and regional left ventricular myocardial deformation measures by magnetic resonance

feature tracking in healthy volunteers: comparison with tagging and relevance of gender. *Journal of Cardiovascular Magnetic Resonance* 2013; **15**(1):8.

32. Evangelista A, Nardinocchi P, Puddu P, Teresi L, Torromeo C, Varano V. Torsion of the human left ventricle: experimental analysis and computational modeling. *Progress in biophysics and molecular biology* 2011; **107**(1):112–121.

33. Bovendeerd PH, Kroon W, Delhaas T. Determinants of left ventricular shear strain. *American Journal of Physiology-Heart and Circulatory Physiology* 2009; **297**(3):H1058–H1068.

34. Nardinocchi P, Puddu P, Teresi L, Varano V. Advantages in the torsional performances of a simplified cylindrical geometry due to transmural differential contractile properties. *European Journal of Mechanics-A/Solids* 2012; **36**:173–179.

35. Taber L. *Nonlinear theory of elasticity: applications in biomechanics*. World Scientific Singapore, 2004.

36. Mehmel H, Stockins B, Ruffmann K, Von Olshausen K, Schuler G, Kübler W. The linearity of the end-systolic pressure-volume relationship in man and its sensitivity for assessment of left ventricular function. *Circulation* 1981; **63**(6):1216–1222.

37. Böl M, Ehret AE, Leichsenring K, Weichert C, Kruse R. On the anisotropy of skeletal muscle tissue under compression. *Acta biomaterialia* 2014; **10**(7):3225–3234.

MOX Technical Reports, last issues

**Dipartimento di Matematica "F. Brioschi",
Politecnico di Milano, Via Bonardi 9 - 20133 Milano (Italy)**

44/2014 PEZZUTO, S.; AMBROSI,D.
Active contraction of the cardiac ventricle and distortion of the microstructural architecture

43/2014 BRUGIAPAGLIA, S.; MICHELETTI, S.; PEROTTO, S.
Compressed solving: a numerical approximation technique for PDEs based on compressed sensing

42/2014 CANALE, A.; VANTINI, S.
Constrained Functional Time Series: an Application to Demand and Supply Curves in the Italian Natural Gas Balancing Platform

41/2014 ESFANDIAR, B.; PORTA, G.; PEROTTO, S.; GUADAGNINI, A.
Impact of space-time mesh adaptation on solute transport modeling in porous media

40/2014 ANTONIETTI, P.F.; MAZZIERI, I.; QUARTERONI, A.
Improving seismic risk protection through mathematical modeling

39/2014 GHIGLIETTI, A.; PAGANONI, A.M.
Statistical inference for functional data based on a generalization of Mahalanobis distance

38/2014 SHEN, H.; TRUONG, Y.; ZANINI, P.
Independent Component Analysis for Spatial Stochastic Processes on a Lattice

37/2014 GIULIANI, N.; MOLA, A.; HELTAI, L.; FORMAGGIA,L.
FEM SUPG stabilisation of mixed isoparametric BEMs: application to linearised free surface flows

36/2014 ABB,A.;BONAVENTURA,L.; NINI, M.;RESTELLI,M.;
Anisotropic dynamic models for Large Eddy Simulation of compressible flows with a high order DG method

35/2014 TRICERRI, P.; DEDE', L.; DEPARIS, S.; QUARTERONI, A.; ROBERTSON, A.M.; SEQUEIRA, A.
Fluid-structure interaction simulations of cerebral arteries modeled by isotropic and anisotropic constitutive laws